Linear-stability investigations for flow-control experiments related to flow over compliant walls

Marcus Zengl and Ulrich Rist

Abstract Results of linear stability calculations and direct numerical simulations for flow-control experiments are presented. Good agreements between measurements and simulations are shown. Furthermore, the linear stability of the flow over the experimental wing section is investigated. Hereby, also the use of isotropic and anisotropic compliant materials is assessed. The prevailing surface-based compliant-wall model of Carpenter was extended to yaw angles, pressure gradients and oblique-traveling disturbances. The influence of the yaw angle is demonstrated for an anisotropy angle of 75°. Also transient-growth of instabilities over the compliant wall was investigated, since the eigenvalue spectrum of the compliant-wall problem turned out to be sensitive to truncation errors. For the parameters investigated, the maximum transient growth of the compliant-wall case is in the same order as the growth of the rigid-wall case.

1 Introduction

For flow-control experiments we investigate the flow of a $1.3m$ long wing section in a wind tunnel. The experiments are conducted by Pätzold et al. at the ILR of the TU-Berlin. The aim of the flow-control experiment is to dampen Tollmien-Schlichting (TS) waves by actively actuating a wall using different control mechanisms. These experiments are inspired by the use of compliant coatings in order to dampen or even inhibit flow instabilities that lead to laminar-turbulent transition. Earlier water tunnel and towing tank experiments found in literature have shown that satisfying transition delays can be achieved. However, since the fluid of the experiment is air, an adequate compliant material does not exist for this purpose. This can be pointed out e.g. by the mass ratio of the compliant coating to the fluid which is in

Marcus Zengl[1] · Ulrich Rist[2]
Institut für Aerodynamik und Gasdynamik, Pfaffenwaldring 21, 70550 Stuttgart, Germany
[1]e-mail: marcus.zengl@iag.uni-stuttgart.de [2]e-mail: ulrich.rist@iag.uni-stuttgart.de

the order of one for the common coatings in water. Therefore, the wall of the wing section is actively actuated in the present experiment to imitate the behavior of a compliant coating. This has the advantage, that all thinkable material properties can be investigated.

2 Numerical simulation of the boundary layer over the wing section

In order to investigate the stability properties of the wing section in the wind tunnel a direct numerical simulation (DNS) of the boundary layer flow was carried out. The key feature of this simulation is that its free-stream and inflow boundary condition (BC) was chosen using the measured free-stream velocity distribution. Therefore, the simulation depends on a high quality of the measurements. This distribution was quantified in one Prandtl tube and two hotwire measurement campaigns. A 9^{th}-order polynomial was then fitted to have the least squares difference to the measurement points and applied for the free-stream velocity of the simulation. The respective free-stream velocities are plotted in Fig. 1 over the downstream coordinate. Furthermore,

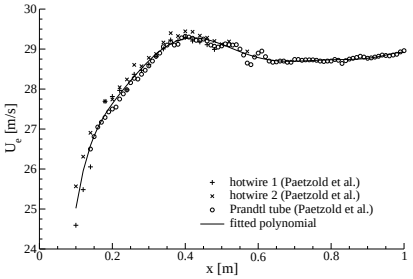

Fig. 1 Comparison of free-stream velocity between experiment and DNS.

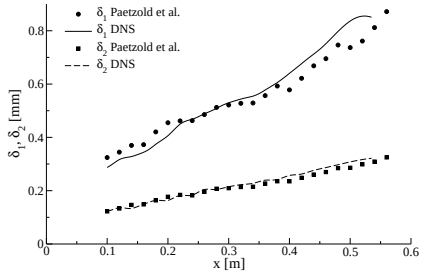

Fig. 2 Comparison of displacement and momentum thickness between experiment and DNS.

velocity profiles were measured by Pätzold et al. at different streamwise positions using a hotwire. The wall-normal spacing of the measurements was $0.1mm$. The inflow velocity profile was chosen such that the momentum thickness matches the momentum thickness of the measurements and that the shape factor matches the local pressure gradient.

To cross-check the simulation data with the experiment, the velocity profiles and integral quantities of the boundary layer were compared. In Fig. 2 the comparison of the displacement and momentum thickness is plotted versus the streamwise coordinate for the laminar part of the boundary layer. Here, the boundary layer thickness

is in the order of a millimeter. Keeping in mind that the boundary layer is very thin, the experimental and numerical data is in good agreement.

To further scrutinize the agreement of experimental measurements and numerical investigations, a comparison of controlled disturbances was conducted. For this purpose a two-dimensional TS-wave of 500Hz was forced by a blowing and suction slot in the front part of the wing section. Downstream the disturbances in the boundary layer were measured by Pätzold et al. using hotwire anemometry at different streamwise locations and wall-normal positions. The measurement data were then evaluated by the authors. Since the time signal of the forcing was measured simultaneously, the phase of different wall-normal measurements could be related. The voltage fluctuations were converted to velocity fluctuations and then Fourier transformed. This permits to extract the eigenfunctions of the generated TS-wave as well as the quantification of the background disturbances. According results are plotted in Fig. 3. The eigenfunctions of the linear stability theory are scaled in their amplitude to match the experimental curves best.

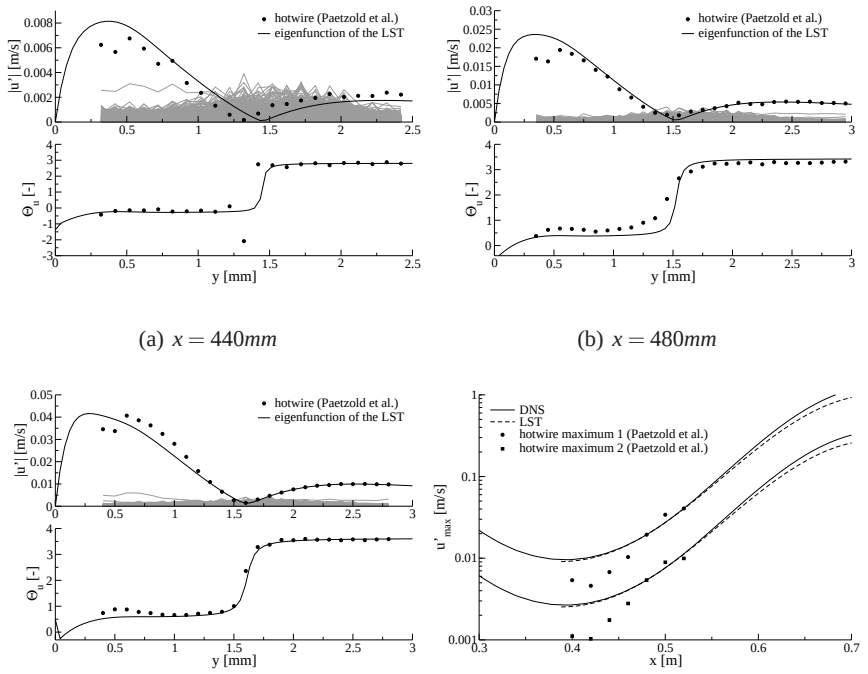

(a) $x = 440mm$ (b) $x = 480mm$

(c) $x = 520mm$ (d) spatial growth

Fig. 3 Comparison of disturbance amplitude and phase at different positions as well as the spatial growth of a TS-wave with a frequency of 500Hz between the experiment and linear stability calculations.

The amplitude and phase of the forced TS-wave are plotted versus the wall-normal coordinate in Fig. 3(a) for $x = 440mm$. The amplitudes of the other resolved frequencies are plotted in gray as a reference to get an idea of the disturbance background. The magnitudes of both, the background disturbances and the forced TS-wave, are of the same order. The amplitude and phase of the forced disturbance do not match well to the linear stability results.

At $x = 480mm$ the agreement between experiment and LST is much better. This is plotted in Fig. 3(b). Here the background disturbances are a magnitude smaller than the forced TS-wave. The amplitude only deviates at the points closest to the wall. The region closest to the wall is very sensitive to small vibrations of the hotwire, because here the velocity gradient is highest. Also the mean velocity is very low so that free convection could deteriorate the results. In the region of the phase shift, small differences in the phase can be ascribed to the low amplitude ratio with respect to the background noise in this region.

In Fig. 3(c) is the comparison for $x = 520mm$. The amplitude of the forced wave is further increased with respect to the background disturbances. In the outer region amplitude and phase are in good agreement with the eigenfunction of the LST. In the inner region the amplitude distribution is different. This is a sign for three-dimensionality. The two-dimensional wave is unstable to three-dimensional disturbances and deforms. Shortly downstream of this location, the laminar flow breaks down making comparisons to the linear theory futile.

In Fig. 3(d) a comparison of the streamwise disturbance-amplitude development between the measured disturbance, DNS and LST is shown. Two criteria were used to define the amplitude. One is the inner maximum of the amplitude distribution, and the other is the outer maximum. The amplitudes of the LST and DNS were scaled to match at the point where the eigenfunctions matched best. Small deviations between LST and DNS are due to nonparallel effects.

The comparison of the controlled disturbance shows that a qualitative comparison is feasible. Keeping in mind that the presented disturbance measurements are in the order of 0.03% of the free-stream velocity, while the displacement thickness is in the order of $0.6mm$ the comparison to the experiment is satisfactory. The base-flow of the DNS can be used to calibrate and design flow control algorithms. Also it enables us to investigate the potential of different compliant-wall parameters.

3 Extended Anisotropic Wall Model

Inspired by the compliant skin of delphinidae a surface-based model of a compliant wall is implemented in the linear stability theory. Pavlov[6] investigated the skin of harbor porpoise and came to the result that its compliant skin not only behaves anisotropic but also its dermal ridges make an angle to the surface stream line. Carpenter et al. developed an anisotropic compliant wall model[3], and implemented it in a framework for two-dimensional disturbances. In our implementation the anisotropic wall model of Carpenter is extended to account for three-dimensional

disturbances and a yaw angle of the material. Furthermore, our implementation is suited for flows with pressure gradients, because an inflection point of the streamwise velocity is not assumed at the wall.

The solution of the linear stability equations—the Orr-Sommerfeld and the Squire equation—using our extended anisotropic wall model differs from the solution for a rigid wall. The boundary condition of the Orr-Sommerfeld equation contains the variable of the Squire equation. Therefore, the classic way of solving the Orr-Sommerfeld equation first and then solving the Squire equation to obtain the eigenfunction is not feasible. Both equations are coupled and have to be solved in combination.

In Fig. 4 is a sketch of the extended anisotropic compliant wall model. A flexible plate is bound to a rigid base with stiffeners. Springs and dampers are attached to the stiffeners. These form an angle θ to the base and an angle ψ to the flow direction. A sectional sketch of the deformed wall is shown in Fig. 5. The cross section has the angle ψ to the flow direction. Note the longitudinal stretch of the flexible plate which is visible by varying distances between its attachment points to the stiffeners. This stretch is induced by the differential motion of the swivel arms, leading to a restoring force to the original form.

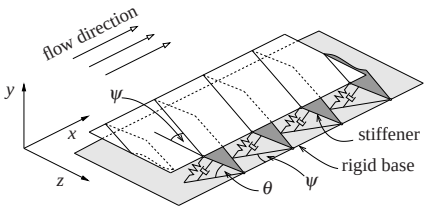

Fig. 4 Sketch of the compliant-wall model.

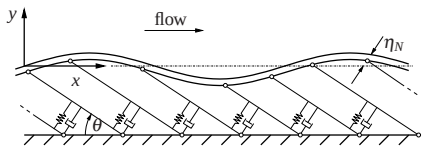

Fig. 5 Sectional view of the wall model.

The wall parameters can be reduced to the non-dimensional quantities

$$C_{\mathrm{m}}^{(\nu)} = \frac{\rho_{\mathrm{m}} b_{\mathrm{m}} U_\infty}{\rho \nu}; \quad C_{\mathrm{k}}^{(\nu)} = \frac{K_{\mathrm{m}} \nu}{\rho U_\infty^3}; \quad C_{\mathrm{b}}^{(\nu)} = \frac{E_{\mathrm{m}} b_{\mathrm{m}}^3 U_\infty}{12\left(1-\nu_{\mathrm{m}}^2\right)\rho \nu^3}; \quad C_{\mathrm{i}}^{(\nu)} = \frac{E_{\mathrm{m}} b_{\mathrm{m}}}{\rho \nu U_\infty} \,. \tag{1}$$

These coefficients account for the *mass ratio* C_{m}, *spring stiffness* C_{k}, *flexural rigidity* C_{b}, and the *induced tension* C_{i} in the plate, caused by the differential motion of the swivel arms. The wall parameters are reflected by *Young's modulus* E_{m}, *Poisson's ratio* ν_{m}, *plate density* ρ_{m}, *plate thickness* b_{m}, and the *spring stiffness* K_{m}. The flow parameters are reflected by *fluid density* ρ, *kinematic viscosity* ν and the *reference velocity* U_∞. The parameters for the calculations presented in this paper are listed in Table 1. Since there is an abundance of possible parameters the present wall parameters were taken from Carpenter[3]. They were optimized to reduce the amplification of TS-waves, while flow-induced surface instabilities (FISI) are kept stable.

Table 1 Compliant wall parameters of the investigated compliant materials.

material	θ	ψ	$C_{\mathrm{m}}^{(\nu)}$	$C_{\mathrm{k}}^{(\nu)}$	$C_{\mathrm{b}}^{(\nu)}$	$C_{\mathrm{i}}^{(\nu)}$
1	0°	0°	1.464×10^{4}	4.443×10^{-5}	1.208×10^{12}	—
2	60°	0°	2.211×10^{3}	7.405×10^{-6}	1.529×10^{9}	2.814×10^{3}
3	75°	0°	5.777×10^{2}	1.983×10^{-6}	2.281×10^{7}	6.152×10^{2}
4	75°	36°	5.777×10^{2}	1.983×10^{-6}	2.281×10^{7}	6.152×10^{2}
5	75°	54°	5.777×10^{2}	1.983×10^{-6}	2.281×10^{7}	6.152×10^{2}
6	75°	90°	5.777×10^{2}	1.983×10^{-6}	2.281×10^{7}	6.152×10^{2}

4 Numerical Implementation of the Linear Stability Equations

For the solution of the Orr-Sommerfeld and Squire-equation we use two numerical schemes. One scheme formulates the equations as a boundary value problem. These are then solved with a *shooting method*. The other scheme formulated the equations as an eigenvalue problem. Here the eigenvalues of a matrix are solved, so we will refer to it as *matrix method*. Both schemes have their specific advantages and disadvantages. The shooting method solves for one eigenvalue/mode using an initial guess. Its computational expense is proportional to the number of used discretization points. It suits well to calculate eigenvalues and eigenfunctions with a high accuracy. Also it can be used to calculate "three-dimensional" stability diagrams, i.e. diagrams with varying parameters *streamwise wavenumber* α, *spanwise wavenumber* β and streamwise location x in a matter of minutes to high accuracy. The matrix method solves for all eigenvalues at the same time. This ensures that no instability mode can be missed. Its computational expense is proportional to the number of discretization points to the power of three. It suits well to calculate transient growth of disturbances. Also its eigenvalues can be used as an initial guess of the shooting method.

The "shooting-method" The stability equations are formulated as in [5, sect. 2.5.2]. This has the advantage that the baseflow appears in the equations only with its first derivative. In the free-stream the three base solutions of parallel flow which decay towards infinity are prescribed. The six first-order equations are then integrated from the free-stream to the wall using a standard Runge-Kutta scheme. The baseflow of the semi-steps is interpolated using a cubic spline. Hence the baseflow can also be non-equidistant. Since the three integrated base solutions grow towards the plate with different growth rates, truncation errors of the slower growing solution grow with higher rates and pose a numerical problem. This problem is overcome by a technique proposed by[4]. After a given number of Runge-Kutta steps the three base solutions are orthonormalized to eliminate the numerical errors. At the wall the base solutions are then combined to fulfill two of the three boundary conditions. The residual of the third boundary condition is then minimized using common root-finding techniques, such as the Newton-Raphson or the Müller method. Note that for these two methods the residual of the boundary condition must be an analytic function of the eigenvalue α or ω that is solved for, but the phase of this complex

quantity can be arbitrary if no special precautions are taken. Therefore, we scale the phase of the residual with the phase of the disturbance pressure at the wall. This creates a very good convergence behavior. The trade-off is that the shooting method does not converge to Squire-modes, because their disturbance pressure is zero at the wall. Using the shooting method one can solve for both, the spatial amplification or the temporal amplification using the same algorithms.

The "matrix method" For the matrix method the stability equations are posed as an eigenvalue problem. The equations are formulated in v and ω_y constituting the Orr-Sommerfeld and Squire-equation. We use a pseudospectral collocation method for discretization, using Chebyshev-Gauss-Lobatto points. Special attention has been paid to the calculation of the differentiation matrices. Since the equations contain the fourth derivative, truncation errors have to be avoided wherever possible. The differentiation matrices were set up using the recursion formula of Welfert[10, eq. 7] for the off-diagonal elements, and the "negative sum trick" of Baltensperger[1] for the diagonal elements. The differentiation matrices are afterwards transformed using the rational mapping that is described in Schmid & Henningson[8, sect. A.4]. Currently, incorporating the compliant wall only the temporal model is implemented in the matrix scheme. Even though the temporal problem states a linear generalized eigenvalue problem, the eigenvalue appears in the compliant-wall BC quadratically. Therefore, we linearize the boundary condition, e.g.[9]. The resulting generalized eigenvalue problem is then solved using the QZ-algorithm.

A comparison of the current implementation to Carpenters results[3] is shown in Fig. 6. The neutral stability curve is plotted versus the Reynolds number based on displacement thickness Re_{δ_1}. Results for a rigid wall, an anisotropic compliant material, i.e. $\theta = 0$, and two anisotropic compliant materials are presented. The neutral stability curves are in very good agreement, and validate the present numerical scheme. Note that not only the area encircled by the neutral stability line is reduced, the maximum amplification rate is also smaller. Using anisotropic materials the amplification of TS waves can be reduced even more than using isotropic materials. A

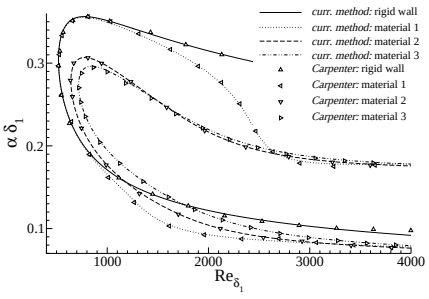

Fig. 6 Comparison of neutral-stability curves.

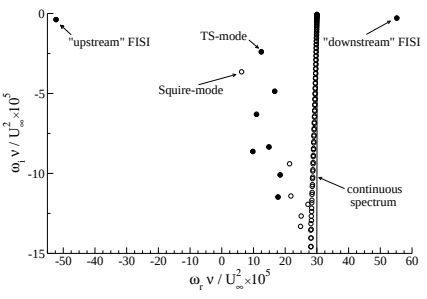

Fig. 7 Eigenvalue spectrum for Blasius flow over material 2 with $Re_{\delta_1} = 1000$, $\alpha = 30\times 10^{-5}\frac{U_\infty}{\nu}$ and $\beta = 65\times 10^{-5}\frac{U_\infty}{\nu}$.

typical eigenvalue spectrum incorporating the compliant wall is shown in Fig.7. The open and filled symbols denote eigenvalues of the matrix method. The filled symbols are eigenvalues found by the shooting method. Note that the shooting method does not converge for the continuous spectrum, since there the residual of the boundary condition is not zero at a discrete location.

5 Further stability investigations of the experimental setup

Stability calculations of the experimental flow were carried out to investigate how far a compliant wall would be able to delay or even inhibit laminar-turbulent transition. Here, again the optimized parameters of Carpenter were used. Note that Pätzold et al. actuate the wall in a small region, and that the following diagrams apply to the case where the surface of the whole wing section is actively actuated. Hence they are somewhat idealized. Values of $U_\infty = 24.5\frac{m}{s}$ and $\nu = 1.54 \times 10^{-5}\frac{m^2}{s}$ were used for the non-dimensionalization of the wall parameters.

Since the Squire-theorem does not apply for growing boundary layers over compliant walls, we have to account for three-dimensional disturbances as well. The maximum spatial amplification rate and the N-factor (i.e. $-\int \alpha_i dx$) is given in Table 2 for the calculations of the different materials. Considerable reduction of both the maximum growth rate as well as the N-factor are achieved by applying the compliant surfaces.

Table 2 Maximum spatial amplification rate and N-factor for the experimental setup.

material	θ	ψ	$\max(-\alpha_i)\,[m^{-1}]$	N
rigid	—	—	9.66×10^{-2}	6.6
1	0°	0°	9.14×10^{-2}	5.4
2	60°	0°	4.31×10^{-2}	2.1
3	75°	0°	4.21×10^{-2}	2.0

Fig. 8 shows a "three-dimensional" spatial stability diagram of the flow in the present experiment. In the spatial model, we prescribe the *angular frequency* ω and the *spanwise wavenumber* β for a given velocity profile at the streamwise location x and solve for the complex *streamwise wavenumber* α. The three quantities x, α and β form the coordinates of the stability diagram. Contours of the *spatial amplification* rate α_i are shown for different slices of the unstable region. The neutral stability surface is pictured with lines of constant spanwise wavenumber β. Since wall and flow are symmetric the stability diagram is also symmetric. It can be seen, that the maximum amplification rate is located at $\beta = 0$. The unstable region is closed at large x, due to the favorable pressure gradient in the rear of the wing section. However, in the wind tunnel experiment the flow becomes turbulent before the end of the unstable region.

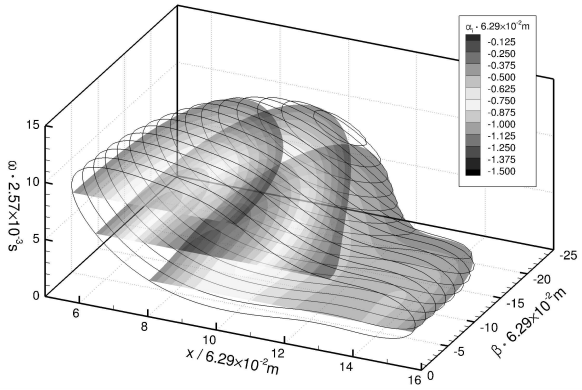

Fig. 8 Spatial stability diagram for the experimental setup with rigid wall.

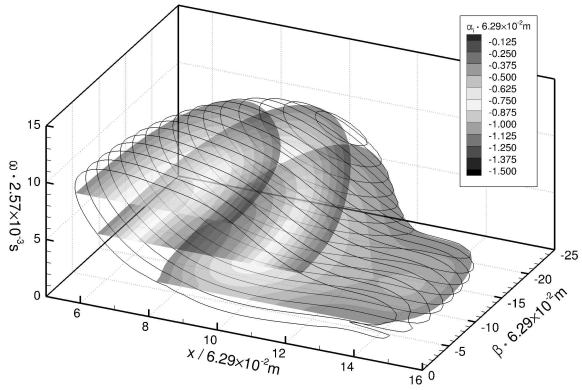

Fig. 9 Spatial stability diagram for the experimental setup with material 1.

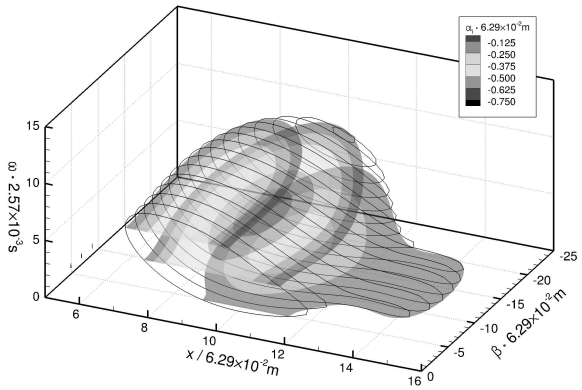

Fig. 10 Spatial stability diagram for the experimental setup with material 2.

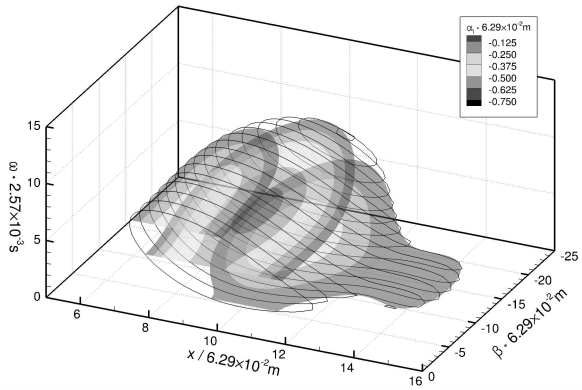

Fig. 11 Spatial stability diagram for the experimental setup with material 3.

Fig. 9 shows a stability diagram for the isotropic material. The unstable region is hardly reduced with respect to the rigid case and the maximum amplification rate is slightly lower. However, the maximum N-factor is reduced from 6.6 down to 5.4. Depending on the disturbance level of the wind tunnel, this reduction could already inhibit the breakdown to turbulence.

When using an anisotropic compliant material, the TS-instability could be further reduced. The stability diagrams for $\theta = 60^\circ$ and $\theta = 75^\circ$ are shown in Fig. 10 and 11 respectively. Here, the unstable region and the amplification rate for two-dimensional waves is significantly reduced. The unstable region for oblique-traveling waves is larger than the one for two-dimensional waves and the maximum amplification rate is located at $\beta \neq 0$. The N-factor is reduced to 2.1 and 2.0 respectively. In the wind tunnel of Pätzold et al. this N-factor leads to inhibition of laminar-turbulent transition. In cases of high free-stream disturbances the breakdown scenario will be different to the rigid-wall case.

The stability diagrams impressively demonstrate that anisotropic compliant walls have a higher potential than isotropic compliant walls to delay or even inhibit laminar-turbulent transition. In case one could actuate the wall of the whole sing section, it would be possible to keep the flow laminar over the entire wing section.

6 Effect of yawing the anisotropic material

It is still not verified if the compliant skin of delphinidae really helps to delay laminar-turbulent transition. Inspired by the work of Pavlov[6] we investigated the effect of yawing the anisotropic material with respect to the flow direction. Pavlov found out that the structures in the epidermis—so-called dermal ridges—make an angle to the flow direction. The effect of this angle was previously unclear. Starting from the materials 2 and 3 we investigated the influence of the yaw angle on the stability properties of the Blasius boundary layer. The results of yawing the material 2 can be viewed in [11]. In this case, the TS-wave with the highest amplification moves from a two-dimensional wave to an oblique-traveling wave. The higher the yaw angle, the higher its spanwise wavenumber. At some yawing angle a FISI becomes unstable traveling in the opposing direction of the TS-wave.

Here we want to show different stages of turning material 3 in more detail. In Fig. 12 a temporal “three-dimensional” stability diagram of the Blasius boundary layer is shown. The neutral stability surface is displayed by lines of constant β. The neutral stability line for $\beta = 0$ is drawn thicker to get an impression how two-dimensional disturbances are affected. Sections of constant α are shaded with contours of the temporal amplification rate. The stability diagram is symmetric with the maximum amplification rate located at $\beta = 0$.

For a yaw angle $\psi = 36^\circ$ the stability diagram is plotted in Fig. 13 The diagram is clearly asymmetric with highest amplification for right-traveling waves. The maximum amplification rate is slightly higher than in the unyawed case. However, two-dimensional waves are more stable.

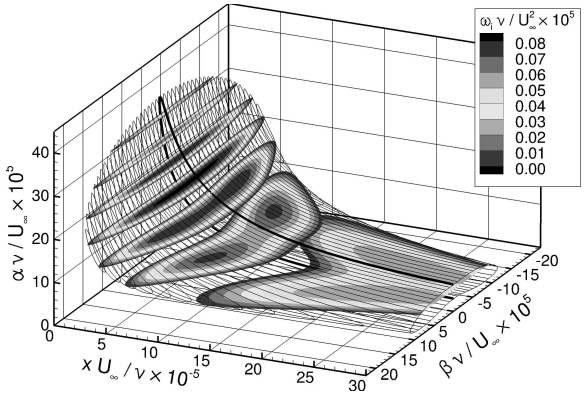

Fig. 12 Stability diagram for Blasius boundary layer over material 3.

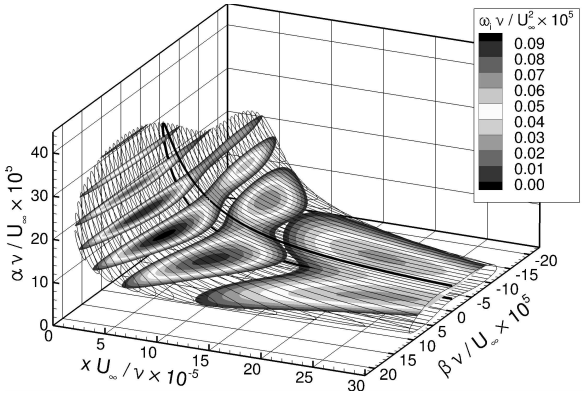

Fig. 13 Stability diagram for Blasius boundary layer over material 4.

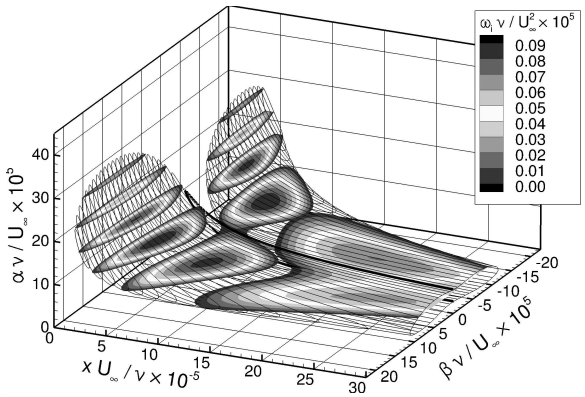

Fig. 14 Stability diagram for Blasius boundary layer over material 5.

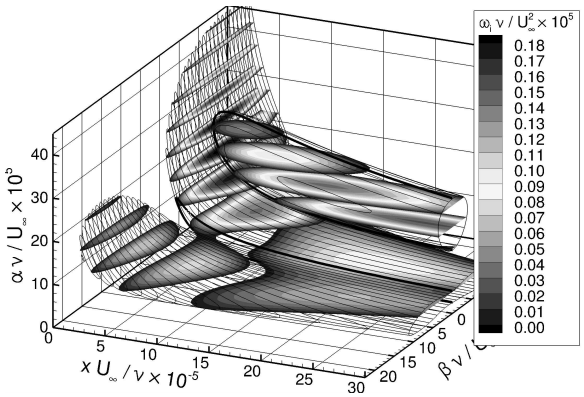

Fig. 15 Stability diagram for Blasius boundary layer over material 6.

With a yaw angle of $\psi = 54^\circ$ two-dimensional waves are significantly more stable. This can be viewed in Fig. 14. Now left-traveling waves are about as amplified as right-traveling waves. The stability diagram has a "symmetry-like" appearance.

Increasing the yaw angle further leads to a destabilization of a FISI-mode. A second unstable region caused by the FISI develops for $\theta = 60^\circ$ as well as for $\theta = 75^\circ$. This can be observed in Fig. 15 for $\psi = 90^\circ$. Here the FISI mode become unstable for two-dimensional waves first. Note that the FISI can become absolutely unstable. It is sufficient to make sure that it is temporally stable at all times to prevent this case which leads to premature transition. For material 6 the amplification rates are significantly higher than for material 3. While turning of the material first promoted right-traveling TS-instabilities, it now promotes left-traveling TS-instabilities.

We conclude that the behavior of the instabilities when yawing the anisotropic material is case dependent. There seems to be no general rule how the single modes are affected. Note that the TS-mode for material 5 and 6 is a formidable example of the invalid Squire-theorem, because it first becomes unstable for oblique waves. It becomes clear that oblique-traveling waves must be taken into account for all stability investigations of compliant walls.

7 Transient growth of disturbances over compliant walls

One distinguishes between the asymptotic stability for long times and the transient stability for short times[7]. Disturbances which are asymptotically stable do not necessarily have to be monotonically stable. Thus, one can imagine disturbances that are asymptotically stable, but grow *transiently* to high amplitudes which cause laminar-turbulent transition. When using the compliant wall model in the LST we encountered a high sensitivity of the eigenvalues to truncation errors. It was previously unclear if this high sensitivity is due to the numerical scheme, discretization or a matter of the physical problem. If the high sensitivity of the problem is caused by the physics, this will be a sign of a high transient growth.

In comparison to the rigid-wall case, a compliant wall causes additional instability modes. In Fig. 7 a typical eigenvalue spectrum of the Blasius boundary layer is plotted for $Re_{\delta_1} = 1000$, $\alpha = 30\times10^{-5}\frac{U_\infty}{\nu}$ and $\beta = 65\times10^{-5}\frac{U_\infty}{\nu}$ and the compliant material 2. One can see two additional modes, which we name "downstream" and "upstream" FISI-mode. These modes have a high wall deformation with respect to their amplitudes, and can have negative phase speeds or phase speeds that are faster than the free-stream velocity. Furthermore, one can see Squire-modes in the spectrum since we solve the Squire-equation in combination with the Orr-Sommerfeld-equation. These also exist for the rigid wall case, but are mostly not solved for, because it can be shown that they are always stable.

To investigate the transient growth of disturbances over compliant walls, we use the method in Schmid and Henningson[8, sect. 4.4]. By superimposing the calculated instability modes we can determine the transient energy of arbitrary disturbances. We use an energy norm that also incorporates the energy of the moving

wall. With some linear algebra, we can optimize disturbances to have the maximum growth within a certain time span τ. Transient energy developments are plotted exemplarily in Fig. 16 for $Re_{\delta_1} = 1000$, $\alpha = 30\times10^{-5}\frac{U_\infty}{\nu}$, $\beta = 65\times10^{-5}\frac{U_\infty}{\nu}$, and a rigid wall. For the three time transients the energy grows highly in magnitude. At the time τ where the initial disturbance was optimized for, the curves touch the curve $G(t)$ tangentially. The curve $G(t)$ is the envelope of all curves. Its maximum exhibits the maximal possible transient growth.

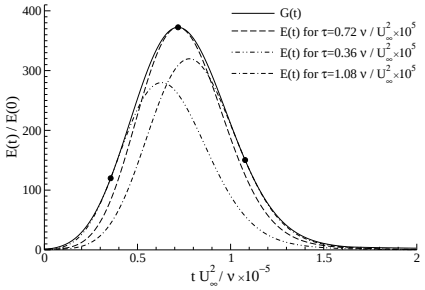

Fig. 16 Time transients of optimal disturbances for Blasius flow over rigid wall with $Re_{\delta_1} = 1000$, $\alpha = 30\times10^{-5}\frac{U_\infty}{\nu}$ and $\beta = 65\times10^{-5}\frac{U_\infty}{\nu}$.

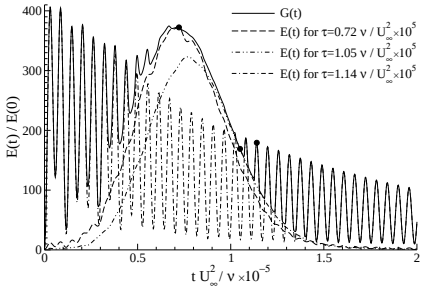

Fig. 17 Time transients of optimal disturbances for Blasius flow over material 2 with $Re_{\delta_1} = 1000$, $\alpha = 30\times10^{-5}\frac{U_\infty}{\nu}$ and $\beta = 65\times10^{-5}\frac{U_\infty}{\nu}$.

In Fig. 17 three transient energy developments are shown for the material 2. The transient behavior has changed dramatically. The envelope $G(t)$ features strong oscillations in wide parts. The curve for $\tau = 0.72\times10^5\frac{\nu}{U_\infty^2}$ shows a similar development as in the rigid-wall case except for a waviness of the curve. For $\tau = 1.14\times10^5\frac{\nu}{U_\infty^2}$ the transient of the energy shows high oscillations and the curve is very close to the envelope in large parts. The frequency of this oscillation correlates with the beat frequency of the two FISI-modes. Since the two modes have a very similar eigenfunction—having their energy in the same wall-normal region—they are non-orthogonal with respect to the energy norm.

This shows that there exists another mechanism for the transient growth of disturbances. Both mechanisms coexist; in different regions either one of them prevails. In Fig. 18(a) contours of the maximum of $G(t)$ are plotted versus α and β for the rigid wall. This plot is in excellent agreement with Schmid & Henningson[8]. The maximum energy growth and its location is listed in Table 3 for the cases we present here. These values for the rigid wall are accurate to 0.2% with respect to the values of Butler and Farrell[2].

In Fig. 18(b) contours of the maximum of $G(t)$ are plotted versus α and β for the anisotropic material 2. The contour plot has changed slightly with respect to the rigid wall case. The location of the maximum transient growth and its magnitude are hardly effected. For large streamwise and spanwise wavenumbers the mechanism of the two interfering FISI prevails. However, the magnitude of this mechanism is in the same order as the classic one. This leads to the conclusion, that the described

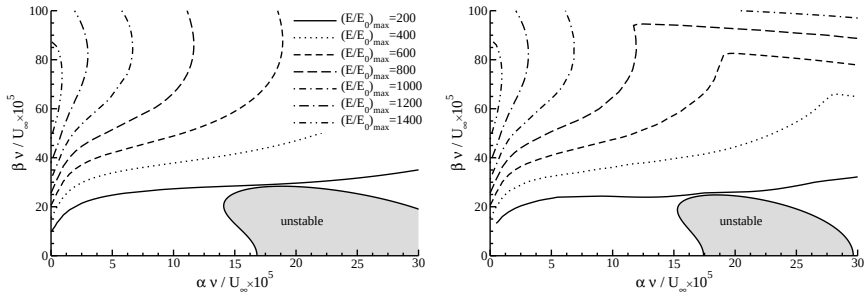

(a) rigid (b) $\theta = 60^\circ$

Fig. 18 Comparison of the maximum transient growth in the Blasius boundary layer at $Re_{\delta_1} = 1000$ for rigid wall and material 2.

Table 3 Maximum transient growth and its location.

material	$G_{\max}$	$\alpha\,(G_{\max})\left[\frac{U_\infty}{\nu}\right]$	$\beta\,(G_{\max})\left[\frac{U_\infty}{\nu}\right]$
rigid	1515	0	6.51×10^{-4}
2	1521	0	6.53×10^{-4}

sensitivity of the eigenvalues to truncation errors is a numerical problem rather than a physical phenomenon. In cases the asymptotic stability can be reduced to low N-Factors by using compliant walls, the effect of transient growth can become an important factor.

8 Conclusion

We have simulated the boundary layer flow over the wing section of the current experiment using direct numerical simulation. The quantitative comparison of the integral quantities of the boundary layer and the comparison of the disturbance development of a forced Tollmien-Schlichting wave has been successful. An extension of Carpenters anisotropic compliant-wall model has been devised and the current numerical schemes are in perfect agreement to results in literature. Investigations of the stability of the flow in the experiment show that if it was possible to actuate the wall of the whole wing imitating the behavior of a compliant coating, laminar-turbulent transition could be inhibited. The introduced yawing of the material with respect to the fluid direction has the effect that the different instability modes are affected in their promoted propagation direction. The results of the calculations show that the Squire theorem is *not satisfied*. Also the the most unstable wave can be a three-dimensional one. We conclude that in-depth stability investigations of compliant walls must take three-dimensional instabilities into account. Though we found

an additional mechanism of transient growth for compliant walls, we have only encountered cases where the energy growth is in the same order as for the rigid wall.

Acknowledgements The authors gratefully acknowledge the financial support by Deutsche Forschungsgemeinschaft (DFG) under the research grant Ri680/18.

References

[1] Baltensperger R, Trummer MR (2002) Spectral differencing with a twist. SIAM J Sci Comput 24:1465–1487, DOI 10.1137/S1064827501388182
[2] Butler KM, Farrell BF (1992) Three-dimensional optimal perturbations in viscous shear flow. Phys Fluids A 4(8):1637–1650, DOI 10.1063/1.858386
[3] Carpenter PW, Morris PJ (1990) The effect of anisotropic wall compliance on boundary-layer stability and transition. J Fluid Mech 218:171–223, DOI 10.1017/S0022112090000970
[4] Godunov SK (1961) Numerical solution of boundary-value problems for systems of linear ordinary differential equations. Uspehi Mat Nauk 16(3(99)):171–174
[5] Mack LM (1984) Boundary-layer linear stability theory. In: Special Course on Stability and Transition of Laminar Flow, AGARD report, vol 709
[6] Pavlov VV (2006) Dolphin skin as a natural anisotropic compliant wall. Bioinspir Biomim 1(2):31–40, DOI 10.1088/1748-3182/1/2/001
[7] Schmid PJ (2007) Nonmodal stability theory. Annu Rev Fluid Mech 39(1):129–162, DOI 10.1146/annurev.fluid.38.050304.092139
[8] Schmid PJ, Henningson DS (2001) Stability and Transition in Shear Flows. No. 142 in Applied Mathematical Sciences, Springer, New York
[9] Tisseur F, Meerbergen K (2001) The quadratic eigenvalue problem. SIAM Rev 43(2):235–286, DOI 10.1137/S0036144500381988
[10] Welfert BD (1997) Generation of pseudospectral differentiation matrices I. SIAM J Numer Anal 34(4):1640–1657, DOI 10.1137/S0036142993295545
[11] Zengl M, Rist U (2010) Linear stability investigations of flow over yawed anisotropic compliant walls. In: Schlatter P, Henningson DS (eds) Proceedings of the Seventh IUTAM Symposium on Laminar-Turbulent Transition, Stockholm, Sweden, 2009, Springer, Berlin, IUTAM Bookseries, vol 18, pp 601–604, DOI 10.1007/978-90-481-3723-7_110